Analysis and design of an inverted oscillating water column for energy storage under choked flow conditions

Antonio Martín-Alcántara[a,*], José Luis Aranda-Hidalgo[b], Alberto Jiménez-Solano[c], Antonio J. Sarsa-Rubio[c]

[a]*Departamento de Ingeniería Eléctrica y Automática, Escuela Politécnica Superior de Córdoba,*
Universidad de Córdoba, Campus de Rabanales, Edif. Leonardo da Vinci, Córdoba, 14071, Spain
[b]*Departamento de Mecánica, Escuela Politécnica Superior de Córdoba,*
Universidad de Córdoba, Campus de Rabanales, Edif. Leonardo da Vinci, Córdoba, 14071, Spain
[c]*Departamento de Física, Facultad de Ciencias,*
Universidad de Córdoba, Campus de Rabanales, Edif. Einstein (C2), Córdoba, 14071, Spain

Abstract

We have investigated a novel idealised system based on the concept of an oscillating water column (OWC) immersed in a mass of water (e.g. in a reservoir or in a pond) as a potential mechanism for energy storage. The system consists of a cylindrical tube separated by a freely moving disk, dividing the device into two chambers. Typically, one chamber contains air and the other water. During the discharge, water enters and contributes to the compression of the air enclosed in the lower chamber. Simultaneously, the compressed air exits the OWC, ideally at atmospheric choked conditions (depending on the design parameters). The device has been conceived for the energy storage during low-price periods, and for the recovery (by executing a discharge e.g. through a turbine) during peak-pricing hours. In this study, we have examined the performance of an inverted OWC (iOWC) at atmospheric discharge (as a first approximation) for different design parameters influencing its performance. We have analysed the performance of the model in terms of the aspect ratio Λ and of the size of the outlet orifice δ, and we have concluded that $\Lambda = 16.5$ and $\delta = 0.0044$ might be a realistic configuration for the practical implementation because (i) the gas is

---

[*]Corresponding author
Email address: `a.martin@uco.es` (Antonio Martín-Alcántara)

choked at the exit orifice (fixing the mass flow rate and pressure at the outlet), and (*ii*) the iOWC's performance is stable (with relatively small oscillations). Additionally, we have provided approximate theoretical solutions for the variables in study, and for the critical time at which choked conditions occur. Finally, as a preliminary step for further analysis involving energy extracting devices at the tank's outlet (e.g. a low-pressure turbine), we have also estimated the maximum initial pressure available when no flow exits the container.

1. Introduction

The unavailability of energy resources and decarbonisation politics have led energy to be one of the primary challenges of our time. The need for cleaner, continuous and storable energy systems is the main direction at which governments are currently aiming at, thrusting energy into the forefront of current research endeavours. Although renewable energy gained significant popularity in the last few years as a potential replacement for fossil fuels, the intermittent generation and the disparity between supply and demand have been promoting the development of efficient energy storage systems. These systems are crucial not only for enhancing renewable energy production but also for optimising conventional sources during periods of substantial pricing variation [1].

In that sense, despite considerable efforts have been made for the development of electric batteries [2], it still remains a limited field affected by several constraints (mainly nature of materials, capacity and temperature). Simultaneously, some different systems have been engineered as viable alternatives for energy storage [3–6]. A promising alternative for energy storage is the use of hydraulic systems [7–9], where turbines, flywheels and accumulators play an important role. Regarding the last ones, e.g. Berrada et al. [10] explored a hydraulic piston device converting (or storing) potential energy upon demand. It consists of a hydraulic circuit driven (or exploited) by a pump (or turbine), connecting a tube with two chambers

separated by a piston. At low-pricing hours, the pump elevates the piston, which at high-demand periods is released to recover energy through a turbine. On the other hand, Van de Ven and Li [11] analysed the operation of a liquid piston device to improve the efficiency of gas compression and expansion. They claimed that the combination of a near-isothermal compression or expansion processes with heat transfer from the gas chamber makes the liquid piston concept advantageous for many applications.

Inspired by the Spanish utility model of Aranda-Hidalgo [12], we present and characterise a novel energy storage device revisiting the well-known oscillating water column (OWC) [13–17] in an inverted way (iOWC). Our approach combines a hydrostatic energy storage (usually during periods of low-priced energy), with a compressed-air discharge, that might be expanded through e.g. a low-pressure gas turbine when required. In contrast to the previous work by Van de Ven and Li [11], the gas compression is performed in the lower chamber to take advantage of the water column weight. The structure of this work is the following: In Sect. 2, we formulate the axisymmetric problem reduced to the 1D non-dimensional, frictionless conservation equations. In Sect. 3, we provide a low-order theoretical solution for the singular perturbative problem. We then identify the parameters governing the iOWC's performance in Sect. 4.1 and conduct a parametric analysis, discussing some relevant cases for the iOWC's implementation (Sect. 4.2). Since oscillatory features have been observed in some cases (depending on the parameters selection), we analyse the effect of dampers of different strengths in Sect. 4.3. Additionally, we explore the iOWC's operation with a closed valve in Sect. 4.4 to determine the maximum compression level that can be reached in case a low-pressure gas turbine is introduced in further studies. Finally, we conclude this study in Sect. 5 by summarising the significant effects of the geometrical aspects on the iOWC's performance and discussing the suitability of the device for real application.

2. Formulation

We are considering the idealised energy storage system displayed in Fig. 1. The device consists of a cylindrical tube that is completely immersed in a fluid mass (usually water) and is vertically oriented. The

tube has a length L and a diameter D. Inside the device, there is a freely moving disk of mass m and negligible width h, which separates the volume into two chambers. The upper contains a progressively increasing (or decreasing) water column, while the lower encloses a compressible gas (typically air) that compresses (or expands), and exits the chamber at atmospheric pressure (for simplicity). The top of the tube is entirely open to allow for water entry, and the air exits the tank through a nozzle orifice of diameter d. This system is idealised to operate on peak-valley energy pricing model, where the disk can be raised
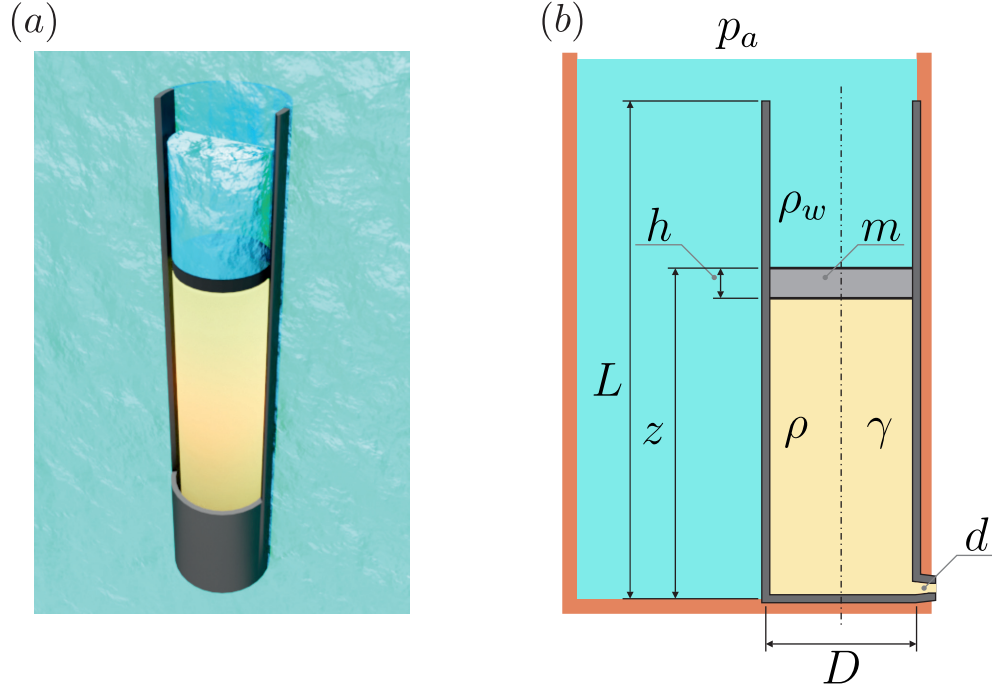

Figure 1: 3D rendered layout of the idealised iOWC (a), system schematic displaying dimensions (b).

during valley hours using an external-powered system (e.g. pneumatic, hydraulic, electric, etc.) to remove the mass of water above it and to introduce the corresponding mass of air at atmospheric conditions. Conversely, the system can be released at peak times, causing the disk to descend and compress the air volume below it.

The operation of the iOWC can be described by the one-dimensional expressions derived from the conservation laws of momentum and mass [Eqs. (1) and (2)] [18], assuming frictionless flow. These equations govern the behaviour of the system and can be respectively written as:

$$m\ddot{z} = -mg - \rho_w g A(L - z) - C\dot{z} + (p - p_a)A, \tag{1}$$

$$\frac{d}{dt}[(z - h)A] = -G, \tag{2}$$

where z is the vertical position, g is the acceleration due to gravity, A is the cross-sectional area of the tube, C a damping coefficient that accounts for wall friction, p is the pressure, and G is the mass flow rate of the air. Note that we have neglected the inertia and the kinetic energy of the water mass entering the system appearing due to the moving control volume (see Reynolds Transport Theorem in e.g. [18]). Additionally, and because we have considered a perfect gas following an isentropic discharge process [18], we can also use the relationship

$$\frac{p}{\rho^\gamma} = \frac{p_a}{\rho_a^\gamma}, \tag{3}$$

with p_a and ρ_a the gas pressure and density at atmospheric conditions, and $\gamma = 1.4$ the adiabatic index for a diatomic ideal gas (e.g. the usual assumption, considering air as a perfect gas).

To describe the gas discharge process in the iOWC (when energy is recovered), we assume that the exit orifice is critical and choked conditions are ideally met during the process [19], i.e.

$$\frac{p}{p_a} = \left(1 + \frac{\gamma - 1}{2}M_s^2\right)^{\frac{\gamma}{\gamma - 1}}, \tag{4}$$

$$G = \rho_s v_s A_s = \sqrt{\gamma\, p\, \rho}\, A_s M_s \left(1 + \frac{\gamma - 1}{2}M_s^2\right)^{-\frac{\gamma + 1}{2(\gamma - 1)}}, \tag{5}$$

where M_s is the Mach number [18] at the tank's outlet. Therefore, by using the isentropic relation Eq. (3)

in Eq. (4) we can express the gas mass flow rate as

$$
G = \begin{cases} \left(\dfrac{2\gamma}{\gamma-1}p_a\rho_a\right)^{1/2} A_s \left[\left(\dfrac{p}{p_a}\right)^{\frac{\gamma-1}{\gamma}} - 1\right], & \dfrac{p}{p_a} \leq \left(\dfrac{\gamma+1}{2}\right)^{\frac{\gamma}{\gamma-1}}, \\[3ex] \left(\dfrac{\gamma+1}{2}\right)^{-\frac{\gamma-1}{\gamma}} (\gamma\,p\,\rho)^{1/2} A_s \left(\dfrac{p}{p_a}\right)^{\frac{\gamma+1}{2\gamma}}, & \dfrac{p}{p_a} \geq \left(\dfrac{\gamma+1}{2}\right)^{\frac{\gamma}{\gamma-1}}, \end{cases}
\tag{6}
$$

with the upper branch representing subsonic conditions and the lower one choked flow.

By using the dimensionless variables [20, 21]

$$
\eta = \frac{z}{L}, \qquad \xi = \frac{p}{p_a}, \qquad \tau = \frac{t}{t_c},
\tag{7}
$$

we have conveniently scaled the expressions Eqs. (1) to (6) to obtain magnitudes of order unity for position, pressure and time, respectively. We can express Eqs. (1) to (6) in the non-dimensional form given by

$$
\frac{d}{d\tau}\left[(\eta-\lambda)\xi^{\frac{1}{\gamma}}\right] \equiv -\mathcal{G} = \begin{cases} a\left(\xi^{\frac{\gamma-1}{\gamma}} - 1\right)^{1/2}, & \xi \leq b, \\[2ex] \xi^{\frac{\gamma+1}{2\gamma}}, & \xi \geq b, \end{cases}
\tag{8}
$$

$$
\alpha\ddot{\eta} + \beta\dot{\eta} = -1 + C_P(\xi-1) - C_A(1-\eta),
\tag{9}
$$

where the different coefficients resulting from the scaling are

$$
\lambda = h/L \ll 1, \; a = \left(\frac{2}{\gamma-1}\right)^{1/2}\left(\frac{\gamma+1}{2}\right)^{\frac{\gamma+1}{2(\gamma-1)}}, \; b = \left(\frac{\gamma+1}{2}\right)^{\frac{\gamma}{\gamma-1}},
$$

$$
\alpha = \frac{L}{g\,t_c^2}, \quad \beta = \frac{CL}{m\,g\,t_c}, \quad C_P = \frac{p_a A}{m\,g}, \quad C_A = \frac{\rho_w L A}{m}.
\tag{10}
$$

The characteristic time has also been chosen to ensure a discharge time of order unity, i.e.

$$
t_c = L\frac{D}{d}\sqrt{\frac{\rho_a}{p_a}}\left(\frac{\gamma+1}{2}\right)^{\frac{\gamma+1}{2(\gamma-1)}}\frac{1}{\sqrt{\gamma}}.
\tag{11}
$$

Equations (8) and (9) need to be solved with the typical initial conditions

$$
\tau = 0, \qquad \eta = 1, \quad \dot{\eta} = 0, \quad \xi = 1,
\tag{12}
$$

6

i.e. at the beginning of the discharge the disk is completely raised and stopped, and the gas chamber is at atmospheric conditions. The discharge is completed at $\eta_f = 1/8$, which has been chosen as a security distance to avoid impacts between the disk and the bottom of the gas chamber.

On the other hand, because we are interested in assessing the performance of the iOWC discharging at atmospheric conditions, it is convenient to consider the potential mechanical energy based on the resulting force F_R on the disk

$$W_m = \int_0^{t_f} F_R \, \dot{z} \, dt, \tag{13}$$

as a figure of merit. It can be expressed in dimensionless form as

$$\mathcal{W}_m = \int_0^{\tau_f} \mathcal{F}_R \, \dot{\eta} \, d\tau \equiv \int_0^{\tau_f} \mathcal{P}_m \, d\tau, \tag{14}$$

with

$$\mathcal{F}_R = -\beta\dot{\eta} - 1 + C_P(\xi - 1) - C_A(1 - \eta) \tag{15}$$

the dimensionless resulting force, and $\mathcal{P}_m$ the mechanical power exerted by the disk. Note that Eqs. (13) and (14) are uncoupled from Eqs. (8) and (9), and it is possible to solve first the system of ordinary differential equations (ODEs) for η and ξ, and then calculate the energy and power that might be recovered during the gas discharge (e.g. through a low-pressure gas turbine at the end of a duct connected to the tank's outlet).

3. Analytical approximate solution

An analysis of the order of magnitude of the coefficients appearing in Eq. (10) indicates that for practical iOWC lengths (to store a reasonable amount of energy) and sufficiently slow discharge times (to avoid structural damage), the value of α must be in general small, leading to a singularly perturbed problem [22]. Furthermore, because we have assumed small wall friction effects for the moving disk, the value of β is also expected to be small. Given these assumptions, we can obtain a zero-order approximation for the

7

solution of Eq. (8) as

$$\eta_0 = 1 - \frac{C_P(\xi_0 - 1) - 1}{C_A}.$$ (16)

To obtain successive approximate solutions for subsonic and choked flow, we can substitute equation (16) into equation (8). It yields (see Appendix A):

$$\xi_0 = \begin{cases} \left(\left(1 + \left[\dfrac{a}{2} \dfrac{\gamma - 1}{\gamma} \dfrac{\tau}{-\chi \left(1 + \frac{1}{\gamma}\right) + \frac{1}{\gamma}\left(1 + \chi + \frac{1}{C_A}\right)} \right] \right)^2 \right)^{\frac{\gamma}{\gamma - 1}}, & \xi \leq b, \\[4ex] b + \dfrac{\tau - \tau_b}{A\, b^{\frac{1-\gamma}{2\gamma}} - B\, b^{\frac{1-3\gamma}{\gamma}}}, & \xi \geq b, \end{cases}$$ (17)

where we have defined the coefficients χ, A and B, to encapsulate the quantities

$$\chi \equiv \frac{C_A}{C_P}, \qquad A \equiv \chi \left(1 + \frac{1}{\gamma}\right), \qquad B \equiv \frac{1}{\gamma}\left(1 + \chi + \frac{1}{C_A}\right)$$ (18)

We can ultimately recover the value of η_0 from Eqs. (16) to (18) using

$$\eta_0 = 1 - \frac{1}{\chi}(\xi_0 - 1) + \frac{1}{C_A}.$$ (19)

Finally, we can use Eq. (17) to determine the critical time τ_b at which subsonic flow transitions to choked flow (see Appendix A),

$$\tau_b = \psi(2b - b^2 - 1) + \phi(b - 1),$$ (20)

where for readability we have defined the coefficients ψ and ϕ,

$$\psi = \frac{1 - \gamma}{4\gamma} A\, b^{\frac{1-3\gamma}{2\gamma}} - \frac{1 - 3\gamma}{4\gamma} B\, b^{\frac{1-5\gamma}{2\gamma}},$$
$$\phi = A\, b^{\frac{1-\gamma}{2\gamma}} - B\, b^{\frac{1-3\gamma}{2\gamma}}.$$ (21)

In terms of energy, we cannot obtain a theoretical approximation for $\mathcal{W}_m$ without higher order corrections because the net force in Eq. (15) is identically zero as we have neglected $\ddot{\eta}$ and $\dot{\eta}$ in Eqs. (16) and (17) at zero-order approximation. Finally, we note from the numerical results in Sect. 4 that different time scales are involved during the discharge process. Therefore, a multiple-scale analysis [20, 23] can be employed in subsequent studies to extend the scope and accuracy of the current approximation.

8

4. Results and discussion

4.1. Dimensional analysis

The equations governing the performance of the iOWC defined in Eqs. (8) and (9) have been integrated numerically in Matlab [24] adopting a 4th-order Runge-Kutta method (ODE45) [25] over a typical range of parameters. In the following, we show the temporal evolution of the state variables η, $\dot{\eta}$ and ξ, and their corresponding phase portraits describing the performance of the device for some cases of interest. The zero-order theoretical solutions obtained in Sect. 3 have been superimposed to the numerical (exact) results to analyse the goodness of the approximation and the range of applicability. Finally, it is worth mentioning that our main goal is to describe the most suitable configuration for the iOWC prototype in terms of energy and maximum power generated.

In order to conduct a proper parametric analysis of the system we have first applied Buckingham's Pi theorem [26] to identify the existing functional relationships between the problem magnitudes. Assuming that the mechanical energy that can be extracted from the iOWC follows the dependence

$$W_m = f\left(L, D, d, g, p_a, \rho_w, \rho_a, \gamma, m, C\right), \tag{22}$$

we can predict the existence of 8 dimensionless parameters, with length, time and mass, the basic magnitudes. If we set D, g and m as linearly independent variables, we can scale Eq. (23) as

$$\frac{W_m}{mgL} = f\left(\frac{L}{D}, \frac{d}{D}, \frac{p_a}{mg}D^2, \frac{\rho_w}{m}D^3, \frac{\rho_a}{m}D^3, \gamma, \frac{C}{m}\sqrt{\frac{D}{g}}\right). \tag{23}$$

For convenience, we have adopted slightly different scales matching the coefficients in Eqs. (8) and (9):

$$\mathcal{W}_m = f\left(\Lambda, C_P, C_A, C_0, \beta, \gamma, \delta\right), \tag{24}$$

with

$$\Lambda = \frac{L}{D}, \qquad \delta = \frac{d}{D}, \qquad C_0 = \frac{\pi\rho L D^2}{m}, \tag{25}$$

9

completing the definitions in Eq. (10). Additionally, because we have introduced the gas density in the characteristic time [see Eq. (11)], we can corroborate

$$\mathcal{W}_m = f\left(\Lambda, C_P, C_A, \alpha, \beta, \gamma, \delta\right). \tag{26}$$

by means of Eq. (10).

4.2. iOWC performance at different discharge regimes

Following the dimensional analysis in Sect. 4.2, we have considered long enough discharge times t_c and negligible wall friction effects (small damping coefficient) ensuring α and β small. This is of course in agreement with the assumptions adopted for the zero-order solution in Sect. 3. Contrarily, the parameters C_A and C_P are typically large because in general $\Lambda > 10$. Thus, we have reduced the parametric study to

$$\mathcal{W}_m = f\left(\Lambda, \delta\right). \tag{27}$$

In Fig. 2 we provide a summary map of the system's mechanical energy in the range of interest

$$2 \times 10^{-3} \leq \delta \leq 5 \times 10^{-2}, \qquad 10 \leq \Lambda \leq 20. \tag{28}$$

From Fig. 2(a) we can observe that δ has a considerable influence on $\mathcal{W}_m$ and that, in general, the larger the exhaust diameter, the higher the energy generated by the system for sufficiently large aspect ratio (say $\Lambda \gtrsim 16$), reaching a maximum value of about 16 at $\Lambda = 20$ and $\delta = 0.05$. On the other hand, note that the maximum power is achieved by combining the smallest orifice size ($\delta = 0.002$) with the largest aspect ratio, as depicted by Fig. 2(b), and it is $\mathcal{P}_m \sim \mathcal{O}(10^4)$. In addition, other effects need to be taken into account for an appropriate design of the prototype. For instance, we have noticed that during a discharge episode the system may exhibit high-amplitude oscillations as a consequence of the relations among the hydrostatic pressure, the mass flow rate at the exit and the gas compression level in the tank. This is illustrated by Fig. 2(c)–(d) in terms of $\mathcal{W}_m(\tau)$ and $\mathcal{P}_m(\tau)$, for some cases of interest that will be discussed in the following. Apart from the oscillations, we can observe that the final time also varies depending on Λ

10

and δ as summarised in Fig. 4, noticing lower energy values at longer discharge times and *vice versa*. On the other hand, the largest mechanical power corresponds to the longest discharge time (with the smallest orifice size). In general, it can be seen that at small aspect ratios, the discharge time depends mostly on Λ
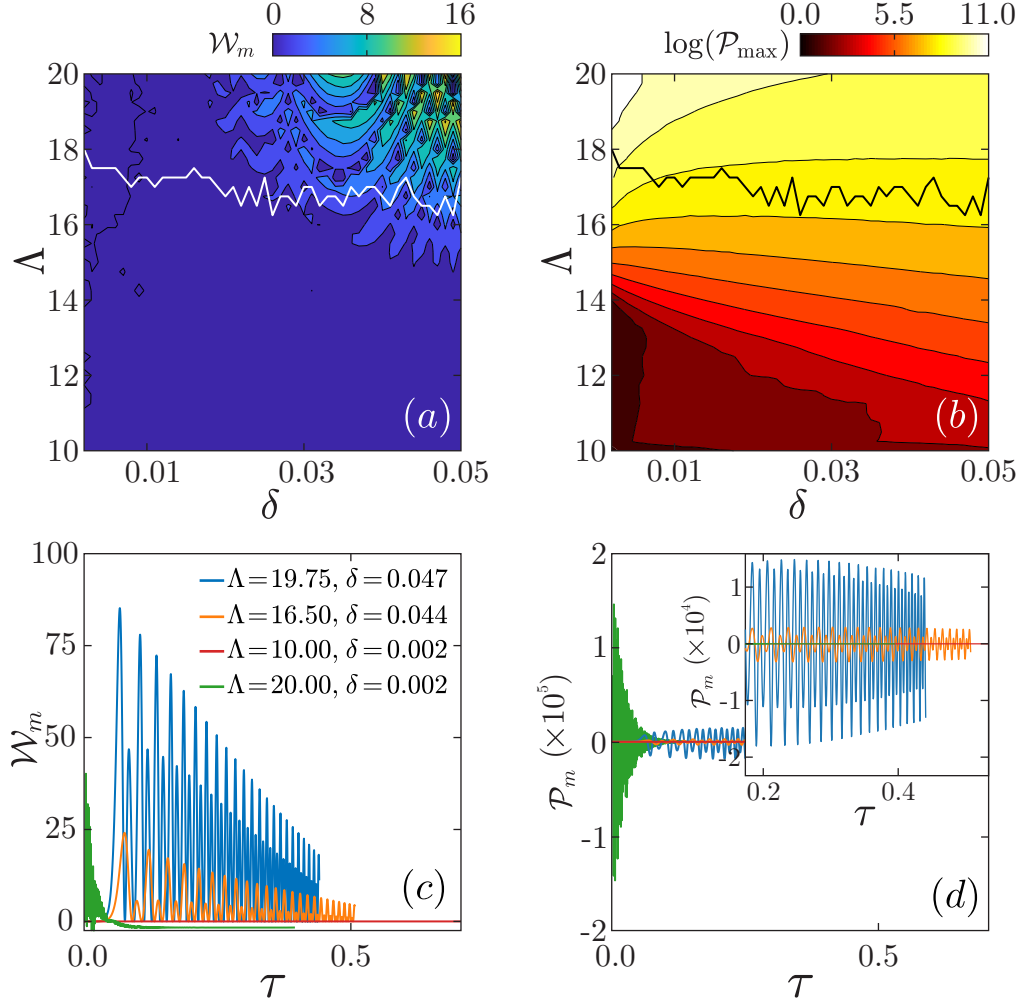

Figure 2: Numerical solutions of $\mathcal{W}_m$ (a) and $\log(\mathcal{P}_{\max})$ (b) for Λ and δ in the range Eq. (30) (white and black solid lines indicate the amplitude oscillation limit with respect to $\tilde{\eta}$). Temporal evolution of $\mathcal{W}_m$ (c) and $\mathcal{P}_{\max}$ (d) for the cases displayed in the legend.
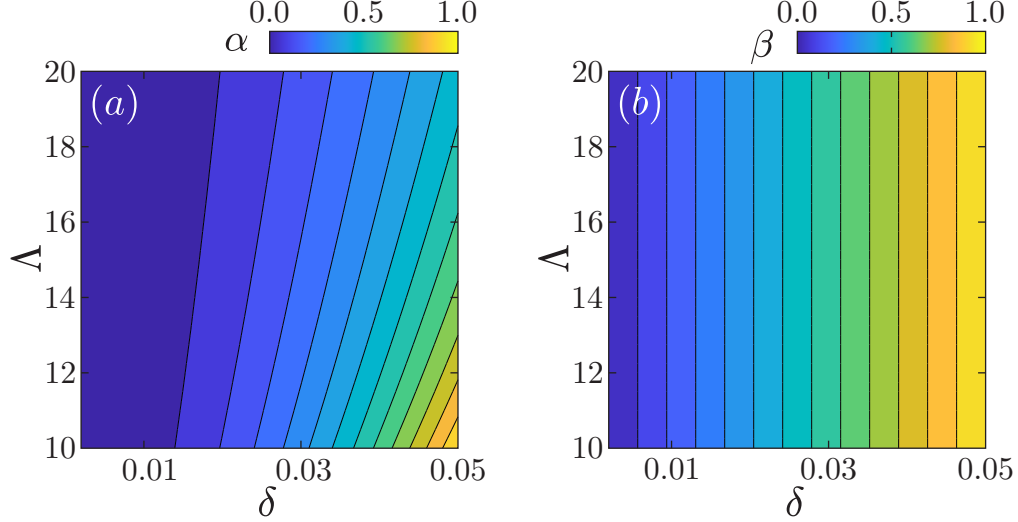
Figure 3: Values of α (a) and β (b) for the range in Eq. (30).

rather than on δ, but as Λ increases, the effect of δ becomes more noticeable. Another noticeable property is the stability of $\mathcal{W}_m$ on Λ or δ. We can see in Fig. 2(c) that a small variation of any of these parameters may lead to a final time, and consequently to a very different final energy. Note that we have obtained completely dissimilar values of $\mathcal{W}_m$ (variations of about ± 25) for the case at e.g. $\Lambda = 19.75$ and $\delta = 0.047$, depending on the discharge time. This effect is also identifiable through the chequerboard pattern on the upper right corner of Fig. 2(a), as the data have not been filtered. Therefore, we find useful to explore the effect of damped iOWC discharges in Sect. 4.2 as an alternative to mitigate system oscillations.

The appearance of oscillations can be explained through the relationship between the parameters C_A and C_P, i.e. the respective weights of hydrostatic and gas pressure terms [see Eq. (8)], with $C_A/C_P \equiv \chi = \rho_w g L/p_a$ maintaining a linear dependence with Λ ($\chi = \Lambda \rho_w g D/p_a$). By analysing the momentum conservation in Eq. (8), we can see that while η and ξ have been scaled to be of order unity, their respective coefficients C_A and C_P in Eq. (10) can grow up to $\chi \simeq 2$ at $\Lambda = 20$. Physically, it means that the hydrostatic pressure acting on the disk compresses the gas contained in the tank rapidly, but at

the same time the discharge is constrained by the outlet choked conditions. The gas reacts immediately, pushing the disk and the water column upwards. These episodes repeat successively until the pressure on both sides of the disk equilibrates. Because we have not yet involved any additional damping mechanism in the system, the oscillations cannot be dissipated quickly and they only fade out depending on the geometrical characteristics (Λ and δ) of the case in study.

To avoid structural damage during the iOWC operation, we have controlled the maximum oscillation amplitude of the disk to be 0.1 with respect to the instantaneous mid-line position $\tilde{\eta}(\tau)$ (the filtered signal itself), discarding the cases that violate this limit. For the estimation of $\tilde{\eta}(\tau)$ we have used a low-pass Butterworth filter [27] of order 8 and cut-off frequency $128/f_s$, with f_s the sampling frequency. We have corroborated that the filter settings remove the oscillations while preserving the solution shape for all the cases in the range of interest in Eq. (28). The solid lines superimposed in Fig. 2(a), (b) display the $\tilde{\eta}$ condition ($\Lambda \lesssim 15$), meaning that we will only consider the iOWC designs below this limit for the practical implementation of the prototype. Accidentally, the values of α and β (see Fig. 3) below this limit are
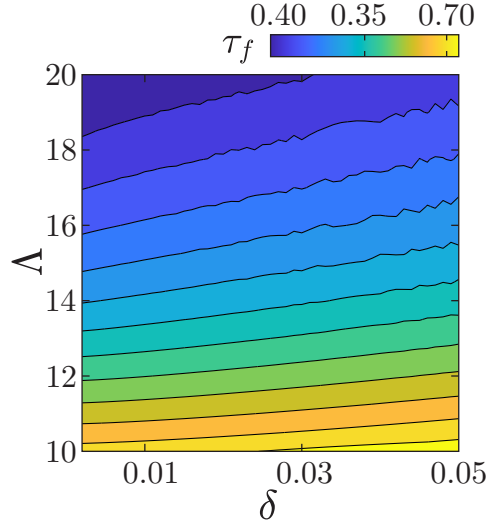

Figure 4: Numerical solution of the final time for each of the cases in Eq. (28).

13

sufficiently small to provide moderate low-order approximations.

Out of the aforementioned (design) region, we analyse first in Fig. 5(a)–(c) the configuration maximising $\mathcal{W}_m$ in Eq. (28), i.e. $\Lambda = 19.75$ and $\delta = 0.047$. Although *a priori* this point could represent the most convenient option (the higher $\mathcal{W}_m$, the better), we observe large oscillations that progressively vanish during the gas discharge. In terms of the disk position, they reach up to a 20% of the amplitude with respect to $\tilde{\eta}$ as depicted in Fig. 5(a), indicating that water alternately enters and exits the upper chamber at a high frequency ($f \simeq 50$), with a maximum peak velocity of $\dot{\eta} \simeq 35$ [see Fig. 5(b)]. This is the main reason that motivates us to obtain choked exit flow in order to disconnect the iOWC's internal dynamics from the constant mass flow rate at the outlet orifice [18, 19]. This feature might be utilised for external
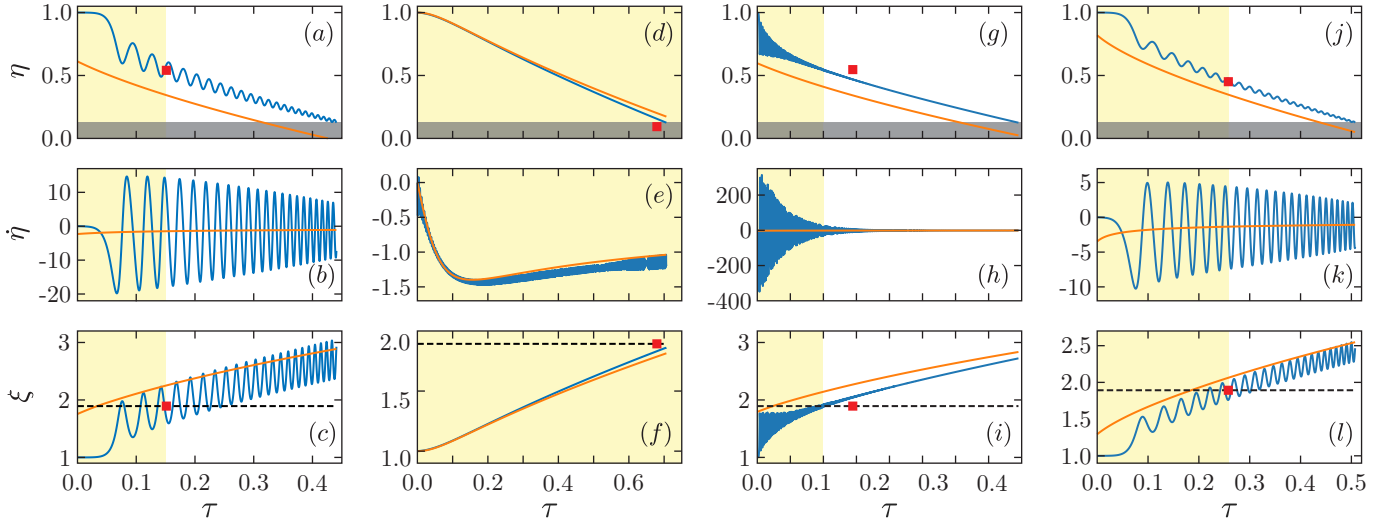

Figure 5: Numerical (blue) and theoretical (orange) temporal evolution of the discharge process corresponding to (a)–(c) $\Lambda = 19.75$ and $\delta = 0.047$, (d)–(f) $\Lambda = 10$ and $\delta = 0.002$, (g)–(i) $\Lambda = 20$ and $\delta = 0.002$, and (j)–(l) $\Lambda = 16.50$ and $\delta = 0.044$. The yellow transparent shading indicates non-choked flow ($\xi < b$), and the grey transparent shading represents the discharge termination position ($\tau_f = 1/8$). The red-filled square markers stand for the theoretical approximation of τ_b in Eqs. (20) and (21). Note that the intersection $\xi_0 = b$ at the bottom row does not coincide with the theoretical value of τ_b because we used a second-order expansion in Eqs. (20) and (21) to improve the accuracy.

14

applications such as a low-pressure gas turbine operating under a steady-state regime. However, even though gas choked conditions rapidly appears at $\tau \simeq 0.15$ and $\eta \simeq 0.6$ in this case [see Fig. 5(a) and (c)], we have considered this geometrical design unsuitable for real implementation because the oscillation limit is clearly exceeded [see Fig. 2(a) and (b)].

Additionally, we have analysed the approximate theoretical solutions of Eqs. (17) to (21) superimposed in Fig. 5(a)–(c). It can be seen that the zero-order approximation is not too accurate compared to the reference (numerical) because the values of α and β are not necessarily small enough in this case (see Fig. 3). Furthermore, the ratio $C_A/C_P \equiv \chi$ reaches the largest value ($\chi \simeq 2$), which results in the high-amplitude oscillations appearing in Fig. 5(a)–(c). This occurs because we have lost one of the initial conditions in addressing the zero-order solution of the singularly perturbed problem after setting $\alpha \to 0$ in the higher-order derivative term $\alpha\ddot{\eta}$ [22]. This effect can be noticed at either $\eta_0(\tau = 0) \neq 1$ in Fig. 5(a) or at $\xi_0(\tau = 0) \neq 1$ in Fig. 5(c). Despite this limitation, and of course admitting that the low-order solution cannot account for the system oscillations (we should go to higher-order corrections), we have reproduced
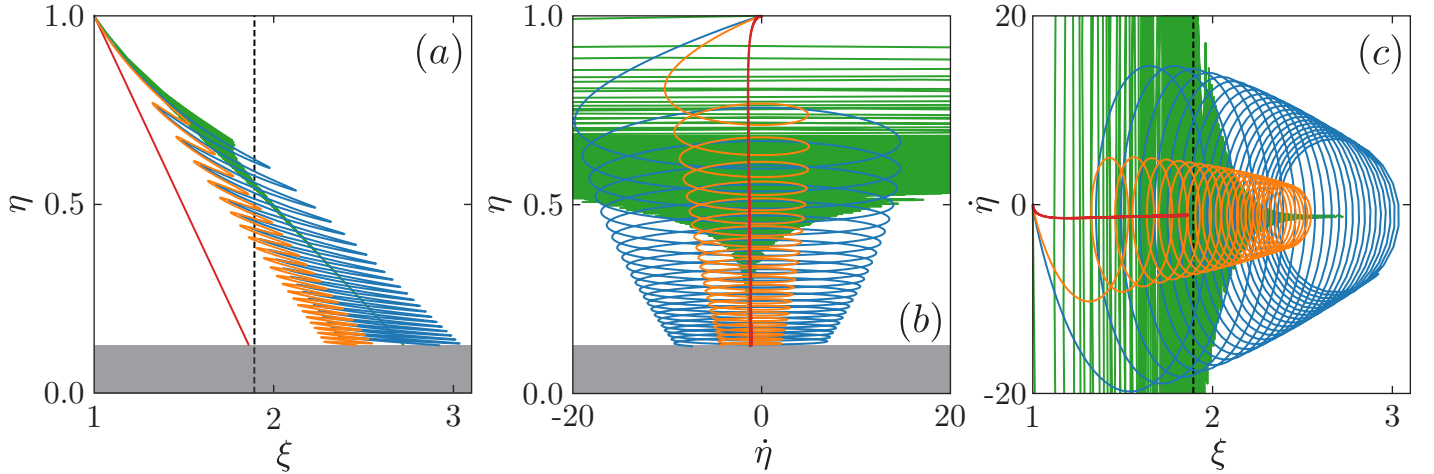

Figure 6: Phase portraits of (a) η vs. ξ, (b) η vs. $\dot{\eta}$ and (c) $\dot{\eta}$ vs. ξ. Same legend as in Fig. 2(b)–(c). Black dashed line indicates $\xi = b$.

15

qualitatively the general trends of $\eta(\tau)$, $\dot{\eta}(\tau)$ and $\xi(\tau)$.

On the other hand, we analyse now the most opposite case corresponding to $\Lambda = 10$ and $\delta = 0.002$, which generates a very small quantity of energy and power Fig. 2(a), (b). Note in Fig. 5(d)–(f) that although stable (not oscillatory) conditions, choked regime is not met at the outlet for this case. Differently to Fig. 5(a)–(c), we can observe that the final time is reached almost twice as late ($\tau_f \simeq 0.7$ vs. $\simeq 0.4$) because the hydrostatic term compensates for the gas pressure ($\chi = 1$), implying that the air is not excessively exposed to compression or expansion episodes, which explains the absence of oscillations. Consequently, the final time practically coincides with that of the discharge [see Eqs. (7) and (11) and Fig. 4] (recall that we are not exactly reaching the final time $\tau_f \simeq 1$ because we are limiting the final state to the height $\eta_f = 1/4$).

In case of sudden power requirements, we expect that the iOWC may generate a rapid incomplete discharge at the most appropriate geometrical conditions, by means of e.g. a morphing discharge orifice. Thus, the largest $\mathcal{P}_m$ value is obtained at $\Lambda = 20$ and $\delta = 0.002$ as it is shown in Fig. 5(d)–(f), corresponding to a very short discharge time in Fig. 2(d). As can be seen in Fig. 2(b) and (d), the power generated by this configuration is larger by far than any of the other cases, at least in one order of magnitude. Unfortunately, although the oscillations have considerably decayed after $\tau = 0.1$ this case still contains high-amplitude fluctuations at high velocities, resulting in large pressure oscillations, as can be noticed in Fig. 5(d)–(f), which violates the security limit on $\tilde{\eta}$ that has been established previously. Also, we can assert that this case does not represent a good choice in terms of energy, as depicted in Fig. 2(a) and (c). Regarding the zero-order approximation, it succeeds in reproducing the trend of the numerical solution, but of course the (quantitative) agreement is not as good as in Fig. 5(d)–(f).

Fixed $\delta = 0.002$, if we increase the aspect ratio up to e.g. $\Lambda = 20$, we can observe in Fig. 2(a) and (c) that this case recovers the smallest energy quantity, but in contrast develops the highest power, as displayed in Fig. 2(b) and (d). If we analyse the temporal evolution of the discharge in Fig. 5(g), we note that the initial transient surpasses the oscillation limit in Fig. 2(a) and (b), with peak-to-peak oscillations about
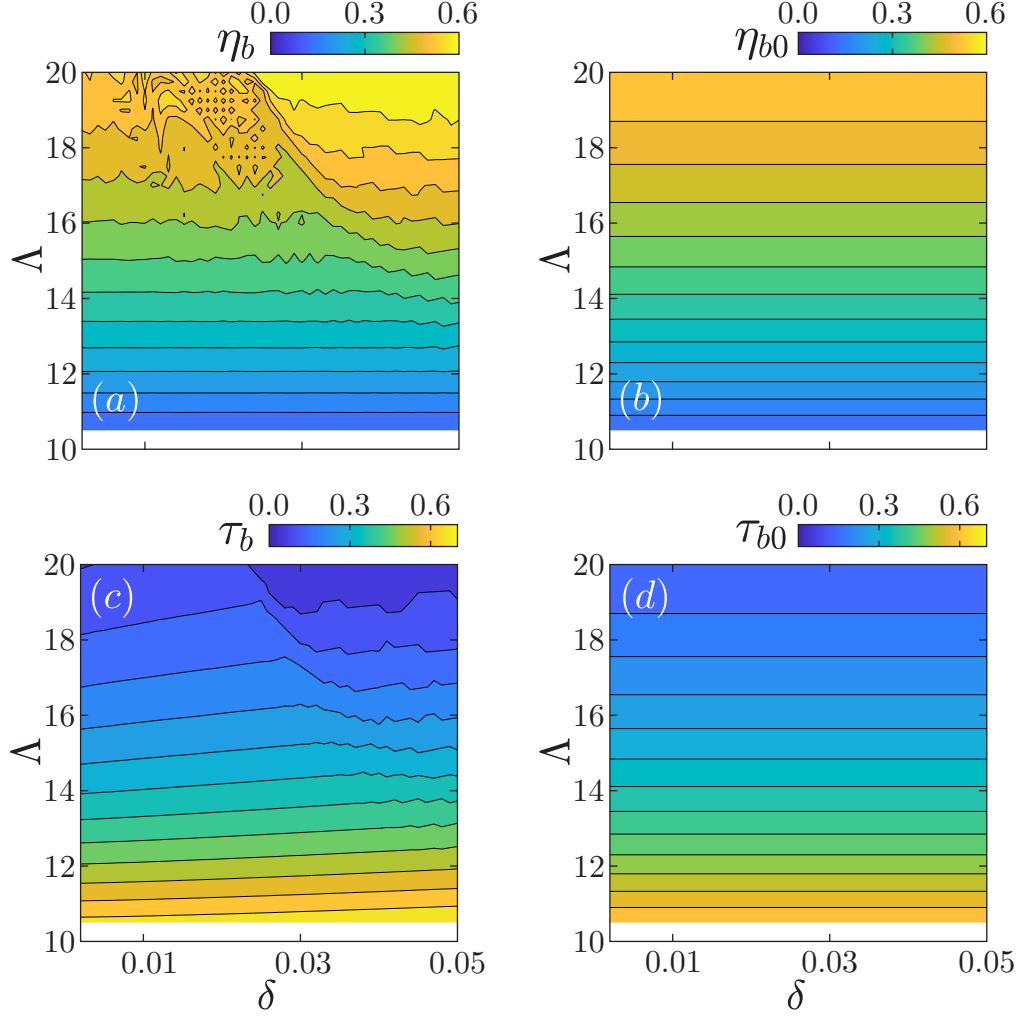
16

Figure 7: Numerical (a) and theoretical (b) solutions of Eq. (20) for the critical time at which choked conditions are met, numerical (c) and theoretical (d) solutions of Eq. (19) for the position at which the critical time in (a) and (b) is reached. Blank spaces indicate unmet choked flow. Subscript 0 on the right-hand side pannels represents theoretical values. The grey transparent shading represents the discharge termination position ($\tau_f = 1/8$).

0.25. Moreover, focused on Fig. 5(h) we appreciate that the velocity peaks have increased considerably (up to two orders of magnitude) with respect to the former configurations Fig. 5(a)–(c) and (d)–(f). Regarding the pressure evolution, it is shown in Fig. 5(f) that choked conditions are reached in a short time ($\tau_b \simeq 0.1$) and the trend is quite similar to that in Fig. 5(c) ($\Lambda = 19.75$ and $\delta = 0.047$). Based on the highly-oscillatory initial transient, we cannot consider either this case a good option for a realistic design of the iOWC. To complete the discussion, we observe that due to the high oscillations, the theoretical approximation suffers from accuracy as happened in Fig. 5(a)–(c), only describing qualitative trend of the numerical solution.

Finally, it is worth discussing the case at $\Lambda = 16.5$ and $\delta = 0.044$, which has resulted to be the most appropriate configuration for the practical implementation of the device. We can see that this case not only generates the maximum amount of energy, as shown in Fig. 2(a) and (c), but we can also clearly see in Fig. 5(j)–(l) that the oscillation peaks are below the $\tilde{\eta}$ limit that we have previously established. As for the analytical approximation, it is depicted in Fig. 5(j)–(l) that this configuration does not provide a very good quantitative agreement, although it is slightly better than that of the former case ($\Lambda = 20$ and $\delta = 0.002$), as it has been depicted in Fig. 5(g)–(i).

In addition to the temporal evolution in Fig. 5, we also explore the phase portraits for the above discussed cases. Figure 6(a) shows the evolution of the gas pressure against the position of the disk, and more interestingly the point where choked flow conditions are developed from (red square for theoretical approximation and transparent yellow shading for the numerical result). Depending on the evolution of η with ξ, we identify different slopes (starting at $\eta = 1$) which relates the gas pressure with the discharge time. In view of Fig. 5 we can asses that a larger negative slope indicates smaller pressure in the tank as a response of a smaller hydrostatic pressure, governed by Λ. Another feature to analyse Figure 6(b) and (c) is the evolution of the disk velocity with the position and the tank pressure. Depending on the discharge orifice we can detect whether $\dot{\eta}$ becomes eventually zero or not. For instance, in the cases at $\delta = 0.002$, the disk velocity damps after an initial oscillatory transient which depends on the Λ size. These

18

velocity fluctuations occurring at $\Lambda \gtrsim 16$, only would represent a practical risk when accompanied of certain amplitude displacements (e.g. above the $\tilde{\eta}$ limit).

For completeness, we summarise the relationship of the parameters Λ and δ with the critical time τ_b and position η_b in Fig. 7, depending on whether the pressure mid-line $\tilde{\xi}$ is larger than the critical pressure b at which choked conditions are met. It is interesting to note the sudden rise and drop taking place in the numerical solution of η_b and τ_b, respectively, at $\delta \simeq 0.30$ and $\Lambda \gtrsim 15$ [see Fig. 7(a) and (c)]. In general, we can observe that the larger the aspect ratio of the iOWC, the more important the gradient on η_b and τ_b. For the range in study $10 \leq \Lambda \leq 20$, we identify these jumps at $0.25 \lesssim \delta \lesssim 0.35$. Out of this region, both η_b and τ_b barely depend on the size of the gas exit orifice. On the other hand, we corroborate that the zero-order theoretical solutions τ_{b0} and η_{b0} in Fig. 7(b) and (d) agree reasonably well with the numerical, especially at not very large Λ quantities. In particular, the theoretical agreement is better at $\Lambda \lesssim 15$, where the quantities $\partial \eta_b / \partial \delta$ and $\partial \tau_b / \partial \delta$ are relatively small (compared to higher aspect ratio cases).

4.3. iOWC performance under damping effects

In the previous section we have studied the performance of the iOWC under undamped conditions (only considering friction between the disk and the walls), which have led to severe oscillations both in power and energy depending on the Λ and δ values in Eq. (28). Consequently, we analyse in this section the effect of a damper for the mitigation of these oscillations, aimed at providing a more realistic operation of the device. We expect that e.g. an electric generator or a dynamo-like apparatus might damp the mechanical oscillations of the iOWC at the same time as they can generate electric energy (the damping energy is partially recovered). On the other hand, if we install a low-pressure turbine at the end of a duct of length comparable to the iOWC's height (L), the pressure drop occurring along would also contribute to smooth the oscillatory effects suffered by the disk inside the tube. Nevertheless, the study of these scenarios would result in a more complicated model that goes beyond the scope of this work and that could be addressed in subsequent studies. Until now, we have considered the influence of a external system through different (larger) values of β. Of course, because we have initially assumed $\beta \ll 1$ for the zero-order theoretical

19

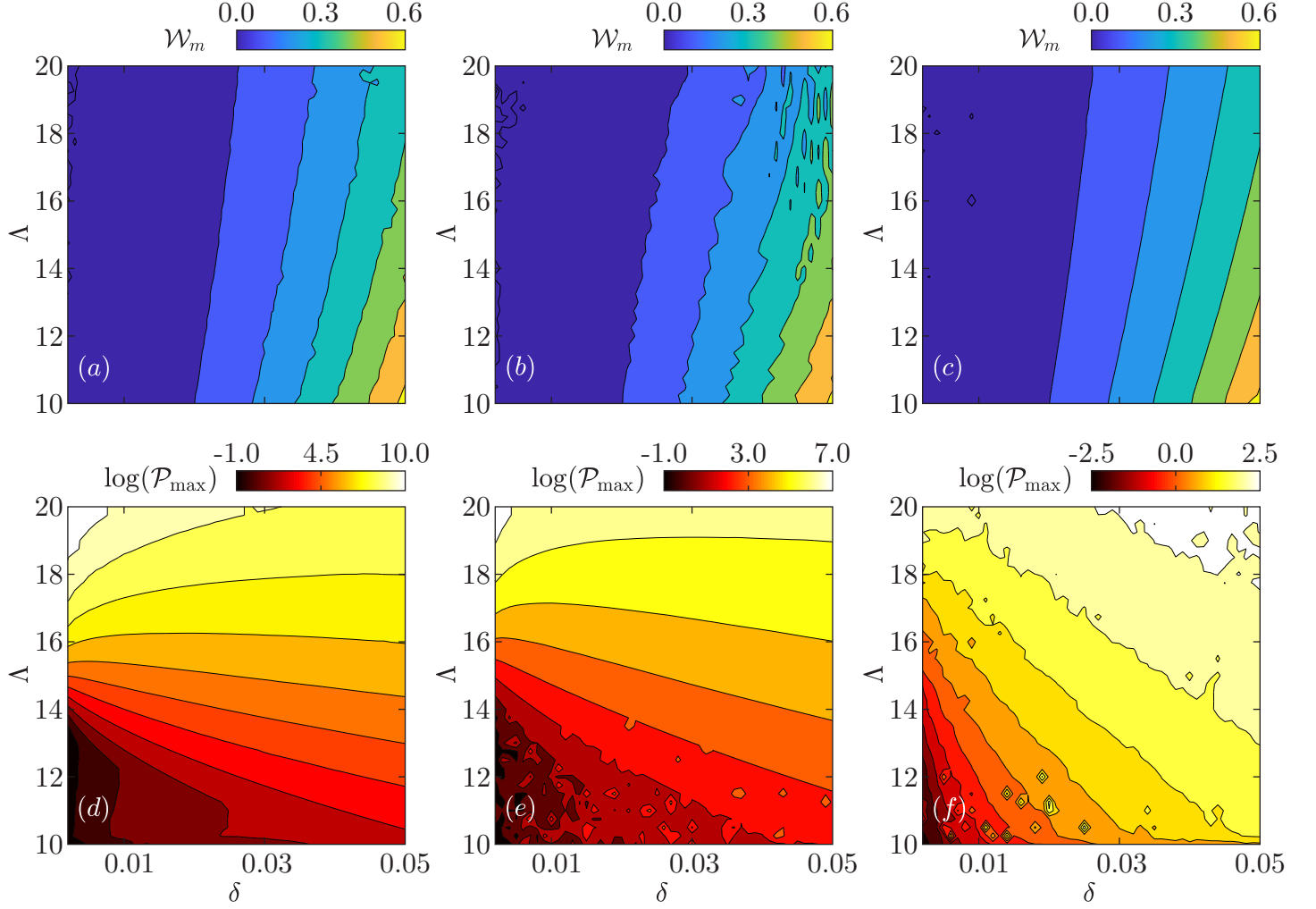solution, we are not providing any analytical approximation violating that assumption.

Figure 8: $\mathcal{W}_m$ (a)–(c) and $\log(P_{\max})$ (d)–(f) for the three different damping coefficients indicated on the top, with $\mathcal{C}_D^0 \simeq 318$.

According to Eq. (10), we can express the non-dimensional, overall damping coefficient as

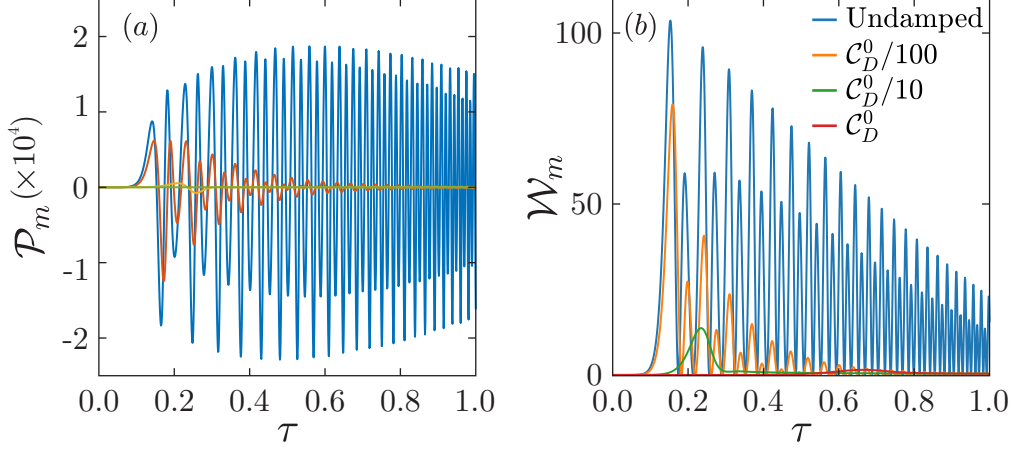$$\mathcal{C}^0 \equiv (C_D + C)\frac{1}{m}\sqrt{\frac{D}{g}}, \tag{29}$$

Figure 9: Scaled temporal evolution of $\mathcal{P}_m$ (a) and $\mathcal{W}_m$ (b) for the case $\Lambda = 20$ and $\delta = 0.05$, and for the different damper strengths shown in the legend.

and consequently

$$\beta = \mathcal{C}^0 \, \Lambda \, \frac{1}{t_c} \sqrt{\frac{D}{g}}. \tag{30}$$

In Fig. 8 we conduct a parametric study on the effect of three different damping values in terms of the evolution of $\mathcal{W}_m$ and $\log \mathcal{P}_{\max}$ during the scaled time (for consistency in the comparison) τ/τ_f. As it could be expected, the larger the damping coefficient the smaller the maximum power provided by the iOWC [Fig. 8(d)–(f)]. However, the magnitude of $\mathcal{W}_m$ seems to saturate at a maximum value of 0.6 from the very first case [see Fig. 8(a)–(c)], which is indeed much smaller than that of the original (oscillatory) case [see Fig. 2(a)]. This effect suggests that even the smallest-strength damper in study compensates for most of the potential energy provided by the water column above the disk, as shown in e.g. Fig. 9 for the highest-amplitude oscillatory case ($\Lambda = 20$ and $\delta = 0.05$). We have detected that at this point, a damping strength of $\mathcal{C}^0/100 \sim \mathcal{O}(1)$ is sufficient to mitigate the oscillations in $\mathcal{W}_m$ from the instant $\tau/\tau_f \simeq 0.6$.

On the other hand, Fig. 10 highlights the existing linear relationship between the damping strength and the final discharge time for the (typical) cases displayed in the legend. In general, we can identify from
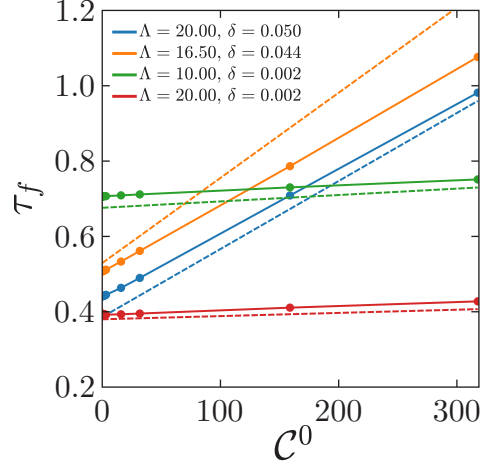
Figure 10: Final discharge time τ_f vs. damper strengths $\mathcal{C}^0$ for the case in Fig. 9. Black dashed line indicates the scaling law $\tau_f/\mathcal{C}^0 \sim \delta/(\Lambda\sqrt{\gamma})$.

the t_c definition in Eq. (11) that $\tau_f/\mathcal{C}^0$ scales pretty well as $\delta/(\Lambda\sqrt{\gamma})$ except for the design case ($\Lambda = 16.5$, $\delta = 0.044$), which further deviates from the numerical results. This scaling law is useful to adequately choose the damper strength for a desired discharge time.

4.4. iOWC performance at zero mass flow rate

In contrast to the previous analyses, and considering that our idealised system might be used to extract energy from e.g. a low-pressure gas turbine, it seems interesting to calculate the highest pressure that can be developed by the iOWC when there is no mass of gas exiting the tank, say in static conditions (at closed valve). This scenario justifies the possibility of reaching a minimal operating pressure $\xi_t > \xi_0 + \Delta\xi$ necessary to operate a low-pressure gas turbine, with ξ_0 the pressure at the tank's outlet and $\Delta\xi$ the pressure drop in a duct. For an initial pressurisation of the gas in the tank we make $\mathcal{G} = 0$ in Eq. (8), resulting

$$(\eta - \lambda)\xi^{\frac{1}{\gamma}} = const., \tag{31}$$

and from the initial conditions $\eta(0) = 1$, $\xi(0) = 1$, we can find the relationship

$$\xi^{\frac{1}{\gamma}} = \frac{1 - \lambda}{\eta - \lambda}. \tag{32}$$

After substitution of Eq. (32) in Eq. (9), we obtain the equation governing the iOWC's performance at closed valve conditions, i.e.

$$\alpha\ddot{\eta} + \beta\dot{\eta} = -1 + C_P \left[\left(\frac{1 - \lambda}{\eta - \lambda} \right)^{\gamma} - 1 \right] - C_A(1 - \eta), \tag{33}$$

which needs to be solved for η. Because we are only interested in the final state of the system, we can directly solve for the steady-state variables η_s and ξ_s, by setting $\ddot{\eta} = \dot{\eta} = 0$. It yields

$$C_P \left[\left(\frac{1 - \lambda}{\eta_s - \lambda} \right)^{\gamma} - 1 \right] - C_A(1 - \eta_s) = 1, \tag{34}$$

where ξ_s can be recovered via Eq. (32) once we have calculated η_S. This nonlinear equation has been solved numerically by adopting the Newton-Raphson algorithm with a general initial guess

$$\eta_s^0 = 1 - \Lambda/100 \tag{35}$$

in the range given by Eq. (28) (of course only involving Λ because the valve is closed).

The contourmap relating the distribution of the available pressure at closed valve with the aspect ratio is shown in Fig. 11. We can observe that for small values of Λ, the gas compression is negligible and pressure remains practically at the very initial value $\xi \simeq 1$. However, at $\Lambda \gtrsim 14$ we notice an increase in the tank pressure as a consequence of the hydrostatic pressure, and so on the disk displacement. We believe that the relationship in Fig. 11 might be of interest for a more complete design of the iOWC because we can determine whether the maximum initial pressure available in the gas tank is sufficient for extracting energy using a low-pressure gas turbine positioned at a given distance from the device. Furthermore, we can determine the initial position at which such pressure level corresponds, and the remaining distance for the discharge.
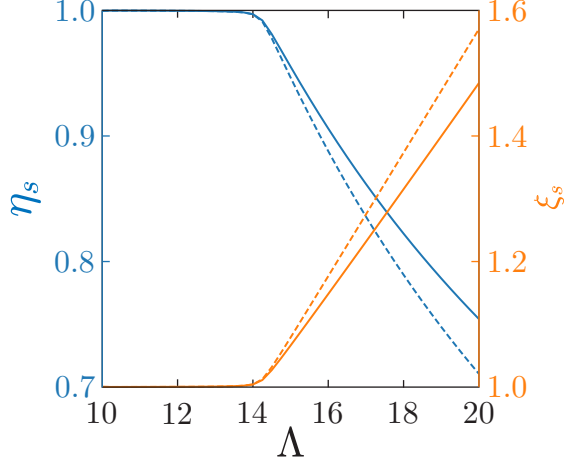
23

Figure 11: Final state solution [see Eqs. (32) and (34)] at closed valve for the range of Λ in Eq. (28).

5. Conclusion

We have analysed in this work a completely innovative mechanism for energy storage based on a cylindrical tank immersed in a mass of water. Although we have only considered atmospheric outlet conditions, we claim that this device holds significant potential for further exploration studies involving expansion through e.g. a low-pressure gas turbine. The inverted oscillating water column is based on the alternate compression and expansion of a gas (e.g. air) in a lower chamber under the action of a mass of water entering into an upper container, both fluids separated by a freely-moving disk. During energy-demand valleys, the disk can be raised by an external powered system, removing the mass of water above it and introducing a given volume of air at atmospheric conditions in the lower chamber, simultaneously. When the energy price increases, one can release the system to recover the potential energy that has been previously stored. In order to determine the optimal geometric relations for the real implementation of the iOWC, we have conducted a parametric study ranging over different values of the aspect ratio Λ and the gas orifice size δ, having computed the mechanical energy and maximum power that can be extracted in each case. During the analysis, we have found some limitations that might be inadequate for the correct

24

operation of the iOWC. For instance, if the hydrostatic pressure is much larger than that of the gas ($\chi > 1$), the device will be exposed to high-amplitude oscillations that may occasion structural damage to the iOWC.

As a main outcome, we present a summary illustrating the mechanical energy that can be extracted from the system based on Λ and δ values. From the temporal evolution and phase portraits of the range of cases in study, we have defined a suitable region that excludes highly oscillatory geometrical configurations, leading to the most appropriate design parameters $\Lambda \approx 16.50$ and $\delta \approx 0.044$. This configurations results in a discharge time of approximately 0.5 units, with choked flow conditions observed at $\tau_b \approx 0.2$ and $\eta_b \approx 0.5$. Apart from the most suitable case, we have compared three additional configurations: (i) Maximum energy extraction ($\Lambda = 19.75$, $\delta = 0.047$), (ii) Maximum power extraction ($\Lambda = 20$, $\delta = 0.002$), and (iii) Reduced oscillations ($\Lambda = 10$, $\delta = 0.002$). In general, choked flow times and their corresponding positions have been reported for all the cases of this work.

On the the other hand, because we might be interested in the mitigation of the oscillations if the iOWC prototype is implemented in real life, we have conducted a sensitivity study on the iOWC performance at three different damping strengths different from the undamped case. This analysis has been limited to exclusively the highest oscillatory case $\Lambda = 20$ and $\delta = 0.002$. The results have revealed that even the smallest-strength damper significantly reduced the energy and power oscillations near the midpoint of the iOWC discharge. However, this reduction has come at the cost of a substantial decrease in the magnitude of $\mathcal{W}_m$ and $\mathcal{P}_{\max}$. In this case, we have mentioned that the use of a dynamo-like device could be interesting to generate energy at the same time that the system is partially (or fully) damped. Additionally, we have found a linear relationship and a corresponding scaling between the discharge time and the damping strength. This law could be useful for the selection of the most appropriate damper given a final discharge time.

Considering our future plans to implement the iOWC coupled with a gas turbine, we analysed the system's solution at closed valve to determine the initial position and maximum pressure for the discharge.

This information is crucial to assess the possibility of choked conditions at the gas outlet, particularly at the beginning of a duct connecting the tank with a low-pressure turbine. Our findings indicate that the maximum available pressure within the range of Λ in study is $\xi_s \simeq 1.5$, but it might be necessary to increase the aspect ratio to achieve higher pressurisation levels if the duct introduces a significant pressure drop. This task will be addressed in future studies.

Finally, we have examined the accuracy of the approximate theoretical solution obtained through regular perturbation techniques for the initial, undamped cases. Because it is a singular perturbation problem, we have found that the theoretical results agree better with the numerical solutions for smaller coefficients α and β. The accuracy of the predictions has also been influenced by the $C_A/C_P \equiv \chi$ ratio, which balances the hydrostatic-to-gas pressure. We have demonstrated that although the zero-order solution is not accurate enough for all the cases that have been analysed, it provides a reasonable trend for some of them. To improve the accuracy of the approximations one should go to higher-order corrections (e.g. through multiple-scales analysis), but the calculation of the zero-order order solution is elaborated enough as to improve it. Indeed, because the computational cost of the numerical simulations is negligible (less than five minutes for the entire range of Λ and δ in a standard personal laptop), our work assumes a well-balanced first approximation.

Data availability

Data will be made available upon reasonable request.

Acknowledgements

Appendix A. Derivation of the theoretical approximate solutions

Appendix A.1. Zero-order unsteady solution at different discharge regimes

In the following, we have derived a zero-order approximation for the subsonic and sonic branches appearing in Eqs. (8) and (9) with the initial conditions in Eq. (12). Inserting Eq. (16) in Eq. (9), we obtain

$$\left[\frac{1}{\chi} \left(1 + \frac{1}{\gamma} \right) \xi^{\frac{1}{\gamma}} - \frac{1}{\gamma} \left(1 + \frac{1}{\chi} + \frac{1}{C_A} \right) \xi^{\frac{1-\gamma}{\gamma}} \right] \dot{\xi} = \begin{cases} a \left(\xi^{\frac{\gamma-1}{\gamma}} - 1 \right)^{1/2}, & \xi \leq b, \\ \xi^{\frac{\gamma+1}{2\gamma}}, & \xi \geq b, \end{cases} \tag{A.1}$$

In the sonic branch ($\xi \geq b$), we can separate the ODE as

$$\left[\frac{1}{\chi} \left(1 + \frac{1}{\gamma} \right) \xi^{\frac{1-\gamma}{2\gamma}} - \frac{1}{\gamma} \left(1 + \frac{1}{\chi} + \frac{1}{C_A} \right) \xi^{\frac{1-3\gamma}{2\gamma}} \right] d\xi = d\tau. \tag{A.2}$$

which has to be solved with the initial condition $\xi(\tau = \tau_b) = b$. After integration, it yields

$$A \frac{2\gamma}{1+\gamma} \xi^{\frac{1+\gamma}{2\gamma}} - B \frac{2\gamma}{1-\gamma} \xi^{\frac{1-\gamma}{2\gamma}} = \tau + C_1, \tag{A.3}$$

standing C_1 for the integration constant, and the constants A and B defined in Eq. (18). If we assume $\xi \sim b + \xi'$, with $\xi' \ll 1$ a perturbation, we can approximate Eq. (A.3) around $\xi = b$ up to $\mathcal{O}(\xi'^2)$ as

$$\left[A b^{\frac{1-\gamma}{2\gamma}} - \frac{1}{\gamma} B b^{\frac{1-3\gamma}{2\gamma}} \right] \xi' + \frac{2\gamma}{1+\gamma} A b^{\frac{1+\gamma}{2\gamma}} - \frac{2\gamma}{1-\gamma} B b^{\frac{1-\gamma}{2\gamma}} = \tau + C_1, \tag{A.4}$$

with C_1 an integration constant. For the linearisation of terms we have used Newton's Binomial theorem, given that $|\xi'/b| < 1$. Using the initial condition $\xi(\tau = \tau_b) = b$, or equivalently $\xi'(\tau = \tau_b) = 0$, we can calculate the value of the integration constant as

$$C_1 = \frac{2\gamma}{1+\gamma} A - \frac{2\gamma}{1-\gamma} B, \tag{A.5}$$

leading to the zero-order solution for the choked flow in terms of ξ,

$$\xi \sim b + \xi' = b + \frac{\tau - \tau_b}{A b^{\frac{1-\gamma}{2\gamma}} - B b^{\frac{1-3\gamma}{2\gamma}}}. \tag{A.6}$$

Alternatively, in order to obtain an approximate solution for the subsonic branch $\xi \leq b$ in Eq. (A.1), we introduce the change of variable

$$\left(\xi^{\frac{\gamma-1}{\gamma}} - 1\right)^{1/2} = u. \tag{A.7}$$

Therefore, we have to solve for u the following first-order ODE:

$$2\frac{u}{\gamma-1}\left[-\frac{1}{\chi}\left(1+\frac{1}{\gamma}\right)(u^2+1)^{\frac{2}{\gamma-1}} + \frac{1}{\gamma}\left(1+\frac{1}{\chi}+\frac{1}{C_A}\right)(u^2+1)^{\frac{2-\gamma}{\gamma-1}}\right] = -a, \tag{A.8}$$

with the initial condition $\xi(\tau=0)=1$, and consequently $u(\tau=0)=0$.

In general, assuming that $u < 1$ is small enough to be considered a perturbation $(u \equiv u')$, and linearising terms around $u = 0$ following Newton's Binomial theorem, we obtain

$$\frac{2}{a}\frac{u}{\gamma-1}\left[\frac{1}{\chi}\left(1+\frac{1}{\gamma}\right) - \frac{1}{\gamma}\left(1+\frac{1}{\chi}+\frac{1}{C_A}\right)\right]u' = \tau, \tag{A.9}$$

and consequently

$$u' \equiv u = -\frac{a}{2}\frac{\gamma-1}{\gamma}\frac{\tau}{-\frac{1}{\chi}\left(1+\frac{1}{\gamma}\right) + \frac{1}{\gamma}\left(1+\frac{1}{\chi}+\frac{1}{C_A}\right)}, \tag{A.10}$$

where terms $\sim \mathcal{O}(u'^2)$ have been dropped out. Note that in this case the integration constant is identically 0 due to the initial condition $u(\tau=0)=0$.

The solution for ξ can be easily recovered after linearisation of Eq. (A.9),

$$\xi \sim 1 + \frac{\gamma}{\gamma-1}u^2. \tag{A.11}$$

Finally, as a further contribution, we provide an approximate solution for the transition time τ_b from subsonic to sonic conditions. Starting from Eq. (A.5), we repeat the linearisation of terms up to $\mathcal{O} \sim (\xi'/b)^3$,

$$\frac{2\gamma}{1+\gamma}A\,b^{\frac{1+\gamma}{2\gamma}}\left[1 + \frac{1+\gamma}{2\gamma}\frac{\xi'}{b} + \frac{1}{\gamma}\frac{(1-\gamma)(1+\gamma)}{8\gamma}\left(\frac{\xi'}{b}\right)^2\right] -$$
$$\frac{1}{\gamma}\frac{2\gamma}{1-\gamma}B\,b^{\frac{1-\gamma}{2\gamma}}\left[1 + \frac{1-\gamma}{2\gamma}\frac{\xi'}{b} + \frac{1}{\gamma}\frac{(1-\gamma)(1-3\gamma)}{4\gamma}\left(\frac{\xi'}{b}\right)^2\right] = \tag{A.12}$$
$$\tau + C_1,$$

which can be expressed in a more compact form as

$$\psi \left(\frac{\xi'}{b} \right)^2 + \phi \frac{\xi'}{b} + K = 0, \tag{A.13}$$

with the value of the coefficients

$$\phi \equiv A\,b^{\frac{1-\gamma}{2\gamma}} - \frac{1}{\gamma} B\,b^{\frac{1-3\gamma}{2\gamma}},$$

$$\psi \equiv \frac{1-\gamma}{4\gamma} A\,b^{\frac{1-3\gamma}{2\gamma}} - \frac{1}{\gamma} \frac{1-3\gamma}{4\gamma} B\,b^{\frac{1-5\gamma}{2\gamma}}, \tag{A.14}$$

$$K \equiv \frac{2\gamma}{1+\gamma} A\,b^{\frac{1+\gamma}{2\gamma}} - \frac{1}{\gamma} \frac{2\gamma}{1-\gamma} B\,b^{\frac{1-\gamma}{2\gamma}}.$$

Through Eqs. (A.13) and (A.14), we have found a solution for the transition time given by

$$\tau_b = \psi(2b - b^2 - 1) + \phi(b - 1). \tag{A.15}$$

Appendix A.2. Final-state solution at zero mass flow rate

We provide an approximation for the algebraic equation in Eqs. (31) to (34). Expanding the tank pressure as

$$\xi_{s0} \sim 1 + \xi'_s, \tag{A.16}$$

where $\xi'_s \ll 1$, we can approximate the position through Eq. (32) by

$$\eta_{s0} \simeq \frac{1}{1 + \frac{1}{\gamma}\xi'_s}, \tag{A.17}$$

where the disk thickness λ has been dropped out for simplicity. After substitution in Eq. (34), we obtain

$$\xi'_s \simeq \frac{1}{2} \frac{C_A}{C_P} - \frac{1}{2} \frac{\gamma}{C_P} \left(C_P - \sqrt{\frac{4\gamma\,C_P + (C_A - \gamma\,C_P)^2}{\gamma^2}} \right), \tag{A.18}$$

and consequently

$$\xi_{s0} \simeq 1 + \xi'_s. \tag{A.19}$$

29

This expression allows us to find out e.g. the iOWC required dimensions to start the gas discharge at a minimum available pressure, and the corresponding position at that pressure level. For the sake of clarity, considering Eq. (10) and the aspect ratio definition $\Lambda = L/D$, we can express the parameter C_A as

$$C_A = \Lambda \frac{\rho_w A D}{m} \equiv \Lambda \hat{C}_A. \tag{A.20}$$

Finally, combining Eq. (A.19) and Eq. (A.20), we can reformulate the solution in Eq. (A.18) as

$$\xi'_s \simeq \frac{1}{2}\hat{\chi}\Lambda - \frac{1}{2}\frac{\gamma}{C_P}\left(C_P - \sqrt{\frac{4\gamma C_P + \left(\Lambda \hat{C}_A - \gamma C_P\right)^2}{\gamma^2}}\right), \tag{A.21}$$

where similar to Eq. (A.19), we have labelled $\hat{\chi} \equiv \hat{C}_A/C_P$ for compactness.

References

[1] A. Olabi, Renewable energy and energy storage systems, 2017.

[2] Y. Yang, S. Bremner, C. Menictas, M. Kay, Battery energy storage system size determination in renewable energy systems: A review, Renewable and Sustainable Energy Reviews 91 (2018) 109–125.

[3] M. S. Guney, Y. Tepe, Classification and assessment of energy storage systems, Renewable and Sustainable Energy Reviews 75 (2017) 1187–1197.

[4] G. Alva, Y. Lin, G. Fang, An overview of thermal energy storage systems, Energy 144 (2018) 341–378.

[5] M. Dalla Via, C. Bianca, I. El Abbassi, A. Darcherif, A thermostatted kinetic theory model for a hybrid multisource system with storage, Applied Mathematical Modelling 78 (2020) 232–248.

[6] M. Ghalambaz, M. Aljaghtham, A. J. Chamkha, A. Abdullah, I. Mansir, M. Ghalambaz, Mathematical modeling of heterogeneous metal foams for phase-change heat transfer enhancement of latent heat thermal energy storage units, Applied Mathematical Modelling 115 (2023) 398–413.

[7] C. Ai, L. Zhang, W. Gao, G. Yang, D. Wu, L. Chen, W. Chen, A. Plummer, A review of energy storage technologies in hydraulic wind turbines, Energy Conversion and Management 264 (2022) 115584.

[8] P. M. Cronk, J. D. Van de Ven, A review of hydro-pneumatic and flywheel energy storage for hydraulic systems, International Journal of Fluid Power 19 (2018) 69–79.

[9] Y. Lin, J. Bao, H. Liu, W. Li, L. Tu, D. Zhang, Review of hydraulic transmission technologies for wave power generation, Renewable and Sustainable Energy Reviews 50 (2015) 194–203.

[10] A. Berrada, K. Loudiyi, I. Zorkani, Dynamic modeling and design considerations for gravity energy storage, Journal of Cleaner Production 159 (2017) 336–345.

[11] J. D. Van de Ven, P. Y. Li, Liquid piston gas compression, Applied Energy 86 (2009) 2183–2191.

[12] J. L. Aranda-Hidalgo, Dispositivo de almacenamiento trienergético trifásico, Utility Model ES-1291145-Y, May 2022.

[13] D. Evans, The oscillating water column wave-energy device, IMA Journal of Applied Mathematics 22 (1978) 423–433.

[14] J. Lighthill, Two-dimensional analyses related to wave-energy extraction by submerged resonant ducts, Journal of Fluid Mechanics 91 (1979) 253–317.

[15] O. Malmo, A. Reitan, Wave-power absorption by an oscillating water column in a channel, Journal of fluid mechanics 158 (1985) 153–175.

[16] Z. Deng, C. Wang, P. Wang, P. Higuera, R. Wang, Hydrodynamic performance of an offshore-stationary owc device with a horizontal bottom plate: Experimental and numerical study, Energy 187 (2019) 115941.

[17] M. Kharati-Koopaee, A. Fathi-Kelestani, Assessment of oscillating water column performance: Influence of wave steepness at various chamber lengths and bottom slopes, Renewable Energy 147 (2020) 1595–1608.

[18] F. M. White, Fluid mechanics, Mcgraw-Hill series in mechanical engineering, 6th ed ed., McGraw-Hill, New York, NY, 2009.

[19] H. W. Liepmann, A. Roshko, Elements of Gasdynamics, Courier Corporation, 2001.

[20] P. Lopez-Tello, R. Fernandez-Feria, E. Sanmiguel-Rojas, Efficient self-propelled locomotion by an elastically supported rigid foil actuated by a torque, Applied Mathematical Modelling 116 (2023) 236–253.

[21] Y. Gao, L. Liu, S. Fu, S. Chai, C. Shi, Nonlinear dynamics of a vertical pipe subjected to a two-phase, solid-liquid internal flow, Applied Mathematical Modelling 120 (2023) 651–666.

[22] J. Kevorkian, J. D. Cole, Perturbation Methods in Applied Mathematics, volume 34, Springer Science & Business Media, 2013.

[23] J. K. Kevorkian, J. D. Cole, Multiple Scale and Singular Perturbation Methods, volume 114, Springer Science & Business Media, 2012.

[24] MATLAB, version: 9.14.0 (R2023a), The MathWorks Inc., Natick, Massachusetts, United States, 2023. URL: https://www.mathworks.com.

[25] L. F. Shampine, M. W. Reichelt, The MATLAB ODE suite, SIAM journal on scientific computing 18 (1997) 1–22.

[26] P. W. Bridgman, Dimensional analysis, Yale university press, 1922.

[27] S. Kaltenbacher, M. Steinberger, M. Horn, Pipe roughness identification of water distribution networks: The full turbulent case, Applied Mathematical Modelling 80 (2020) 879–894.